High Electroresistance in All-Oxide Ferroelectric Tunnel Junctions Enabled by a Narrow Bandgap Mott Insulator Electrode

Yuanyuan Zhang,[1] Yifei Hao,[1] Le Zhang,[1] Kun Wang,[1] Xia Hong[1,2,a)]

[1] *Department of Physics and Astronomy, University of Nebraska-Lincoln, Lincoln, Nebraska 68588-0299, USA*

[2] *Nebraska Center for Materials and Nanoscience, University of Nebraska-Lincoln, Lincoln, Nebraska 68588-0298, USA*

[a)] Author to whom correspondence should be addressed: xia.hong@unl.edu

Abstract:

Ferroelectric tunnel junctions (FTJs) based on epitaxial complex oxide heterostructures are promising building blocks for developing low power nanoelectronics and neuromorphic computing. FTJs consisting of correlated oxide electrodes have distinct advantages in size scaling but only yield moderate electroresistance (ER) at room temperature due to the challenge in imposing asymmetric interfacial screening and large modulation of the tunneling potential profile. Here, we achieve large ER in all-oxide FTJs by paring a correlated metal with a narrow bandgap Mott insulator as electrodes. We fabricate epitaxial FTJs composed of 2.8 and 4 nm $PbZr_{0.2}Ti_{0.8}O_3$ tunnel barriers sandwiched between correlated oxides $LaNiO_3$ and $Sr_3Ir_2O_7$ electrodes. An ER of 6,500% has been observed at room temperature, which increases to over 10^5% at 100 K. The high ER can be attributed to ferroelectric polarization induced metal-insulator transition in interfacial $Sr_3Ir_2O_7$, which enhances the potential asymmetry for the tunnel barrier. The temperature dependence of tunneling current shows that direct tunneling dominates in the on state, while the off-state conduction transitions from thermally activated behavior at high temperatures to Glazman-Matveev defect-mediated inelastic tunneling at low temperatures. Our study provides a viable material strategy for designing all-oxide FTJs with high ER, facilitating their implementation in nonvolatile memories and computing devices.

Ferroelectric tunneling junctions (FTJs) utilize the nonvolatile polarization of a ferroelectric barrier to modulate the tunneling current between two conductive electrodes.[1-3] Due to the voltage-controlled nature and non-destructive readout, FTJs have been considered as a promising building block for developing nonvolatile memories and neuromorphic applications.[4, 5] Compared with FTJs composed of ferroelectric polymers[6] and two-dimensional van der Waal materials,[7, 8] epitaxial complex oxide FTJs have distinct advantages in scalable growth and low switching voltage. The atomically sharp epitaxial interfaces promise low defect states and high homogeneity in comparison with FTJs based on polymorphous oxides.[9-11] It is further conceivable to leverage the unit-cell-scale domain-wall width[12] and fast polarization switching[13, 14] of ferroelectric perovskites and their high quality heterointerfaces with magnetic oxides for building high density, fast speed multiferroic FTJs with potentially multi-level switching.[15, 16] Previous studies of epitaxial complex oxide FTJs have focused on exploiting the scanning probe,[17, 18] metal (*e.g.*, Co, Au, Pt),[14, 15, 19, 20] or 2D material (*e.g.*, graphene and MoS_2)[21, 22] as the top electrode. While all-oxide epitaxial FTJs are desirable for streamlined sample growth and device fabrication, there have been only few studies to date.[23-29]

One of the key challenges in the implementation of all-oxide epitaxial FTJs for high density nanoelectronics is imposed by the competing material requirements for size scaling and high electroresistance (ER). In FTJs, the electrostatic potential asymmetry induced by electrodes with different screening lengths alters the ferroelectric barrier height upon polarization reversal, leading to the ER effect. Adopting electrodes with highly asymmetric screening capacity is thus critical for achieving high ER.[30] In prior studies of all-oxide FTJs, high potential asymmetry has been achieved by pairing a correlated oxide such as (La,Sr)MnO_3 (LSMO) with a semiconducting oxide such as Nb-doped $SrTiO_3$ as electrodes,[27, 29] or inserting a dielectric layer to form a composite tunnel barrier.[26, 28] In the former case, the semiconducting carrier density leads to large depletion width for the electrode,[31] substantially limiting the size scaling potential of the FTJs. For the latter configuration, interfacing an ultrathin ferroelectric with a dielectric layer would lead to severe depolarization field and cause domain formation,[32] compromising the retention and endurance of device switching. As correlated oxides possess high carrier density (10^{21}-10^{23}/cm^3) with sub-nanometer screening length,[33] adopting correlated oxides as both top and bottom electrodes can facilitate size scaling and minimize depolarization field. However, the potential asymmetry in such FTJs is significantly reduced due to the similar screening capacity of various correlated oxides and

the relatively small modulation of carrier density in correlated oxides via ferroelectric polarization,[34, 35] and only moderate ER has been achieved at room temperature (RT).[23-25]

A promising route to enhance the ER in correlated oxide-based FTJs is to pair a Mott insulator with a conductive oxide as electrodes. When the Mott insulator is in the vicinity of the metal-insulator transition (MIT), it is possible for the ferroelectric polarization to induce distinct electronic states in the two oxide electrodes, enabling a high potential asymmetry. For this material scheme, there are two critical considerations for choosing the Mott insulator electrode. First, the ferroelectric polarization should be sufficient to induce a MIT in the interfacial layer of the Mott channel. Second, the insulating state of the Mott channel should have moderate conductivity even in the insulating state to effectively mitigate the depolarization effect.[34, 35] Such constraints can be satisfied by working with a narrow bandgap Mott insulator. The Ruddlesden-Popper series of 5*d* iridates represent a model system where the combination of spin-orbit coupling (SOC) and Coulomb interaction can drive a narrow-gap Mott state. The strong SOC of Ir splits the t_{2g} band into upper J_{eff} =1/2 and lower J_{eff} = 3/2 bands. In $Sr_{n+1}Ir_nO_{3n+1}$, the J_{eff} = 1/2 band of Ir^{4+} ($5d^5$) ion is half-filled, where the on-site Coulomb energy can open a Mott gap. With the bandwidth increasing with n,[36] a narrow Mott gap of about 0.1 eV emerges in $Sr_3Ir_2O_7$ (SIO, n = 2).[36, 37] The ferroelectric field effect can thus be effective in inducing a MIT in $Sr_3Ir_2O_7$. The small bandgap also yields relatively high conductivity in the insulating state of $Sr_3Ir_2O_7$ compared with 3*d* and 4*d* Mott insulators.[38, 39] These properties make it an appealing electrode candidate for constructing all-oxide epitaxial FTJs. The recent observation of light-induced MIT in a narrow-gap Mott insulator[40] further points to the possibilities of realizing multi-state, multi-functional FTJs with $Sr_3Ir_2O_7$ electrodes.

In this study, we report large ER achieved in epitaxial FTJs composed of 2.8 and 4 nm $PbZr_{0.2}Ti_{0.8}O_3$ (PZT) tunnel barriers sandwiched between correlated metal $LaNiO_3$ (LNO) and Mott insulator $Sr_3Ir_2O_7$ electrodes. A large ER of 6,500% has been observed at RT in the FTJ with a 4 nm PZT tunnel barrier. The ER increases with decreasing temperature, reaching over 10^5% at 100 K. The weak temperature dependence of the on-state tunneling current can be well described by direct tunneling, while the off-state conduction evolves from thermally activated behavior at high temperatures to defect-mediated inelastic tunneling at low temperatures. Our study sheds light on the material design of correlated oxide-based epitaxial FTJs with large ER.

We deposited epitaxial LNO/PZT/SIO heterostructures on (001) $(LaAlO_3)_{0.3}(Sr_2AlTaO_6)_{0.7}$ (LSAT) substrates using off-axis radio-frequency magnetron sputtering. Detailed information for sample growth and device fabrication can be found in the Supplementary Material. X-ray diffraction (XRD) measurements reveal (001) growth for all layers with no apparent impurity phases [Fig. 1(a)]. Atomic force microscopy (AFM) images show a typical root-mean-square surface roughness of about 6 Å [Fig. 1(a) inset]. Piezoresponse force microscopy (PFM) measurements taken on a 4 nm PZT/12 nm SIO sample show robust switching hysteresis [Fig. 1(b)], confirming ferroelectricity of the ultrathin PZT layer. We fabricated LNO/PZT/SIO heterostructures into FTJ devices [Fig. 1(c)-(d)] (Supplementary Fig. S1). The electrical characterizations were taken in a Quantum Design Physical Property Measurement System with a Keysight B1500A Semiconductor Characterization System. The results reported are based on one device with 2.8 nm PZT (denoted as J1) and two devices with 4 nm PZT (denoted as J2 and J3).

Figure 1(e) shows the tunneling current I as a function of bias voltage (V_{bias}) taken on junction J1 at RT. We poled PZT to the polarization up (P_{up}) and down (P_{down}) states by applying negative and positive pulse voltages, respectively, exceeding the coercive voltage (V_c) to the top electrode, with the bottom electrode grounded. Switching the polarization of PZT leads to reversible current modulation between two distinct, nonlinear I-V_{bias} states. The P_{up} (P_{down}) state corresponds to higher (lower) tunneling current, defined as the on (off) state. The ER, defined as $(I_{on}-I_{off})/I_{off}$, reaches 280% at V_{bias} = -0.5 V.

To study the switching behavior of the tunneling current, we applied a sequence of pulsed writing voltages (V_{write}) to the junctions and read out the tunneling current at a constant V_{bias} lower than V_c. Figure 2(a) shows the RT tunneling conductance $G = I/V_{bias}$ at V_{bias} = -0.5 V as a function of V_{write} for junction J1. The switching hysteresis exhibits well-defined on and off states with an ER of about 1,000%. The clear decay in the on-state conductance with time explains the lower ER obtained from I-V_{bias} [Fig. 1(e)]. The current relaxation can be related to the depolarization effect in the PZT barrier. As $Sr_3Ir_2O_7$ is an insulator, the screening of ferroelectric polarization is mainly provided by hole-doped $LaNiO_3$.[35] The P_{up} state depletes carriers from interfacial $LaNiO_3$, rendering pronounced depolarization for the on state. At 100 K, the device exhibits significantly higher (lower) on (off) state conductance, with ER increasing to 1.46×10^5%. This can be due to the pyroelectric change of ferroelectric polarization. It has been shown that the polarization of epitaxial PZT thin films increases by about 2.5 μC cm^{-2} from 300 K to 100 K,[41] which can account

for a pronounced change for ultrathin PZT tunnel barriers close to the finite size limit.[42] The much higher V_c and highly square hysteresis loop at 100 K can be attributed to the suppressed domain wall depinning in PZT, which is thermally activated.[43]

We then studied the switching characteristics of junction J2 with a 4 nm PZT barrier [Fig. 2(b)]. The coercive voltages in the *G-V* loops are much larger than those in the PFM switching hysteresis taken on PZT/SIO [Fig. 1(b)], which is understandable given the different electrostatic and mechanical boundary conditions at the top interfaces for the metallic AFM tip (Pt)/PZT and epitaxial LNO/PZT.[44] Similar discrepancies in V_c have been observed in $BaTiO_3$-based FTJs.[45] The device also exhibits nonvolatile switching of tunneling current at RT, with significantly higher ER of 6,500%. Both on and off states do not show apparent decay, with the current levels comparable with those obtained in I-V_{bias} (Supplementary Fig. S2). The enhanced ER and improved retention can be attributed to the thicker tunneling barrier. For direct tunneling dominated FTJs, the ER ratio increases exponentially with the barrier thickness.[17, 18] Moreover, as ultrathin epitaxial PZT films are subjected to the finite size effect, the 4 nm PZT barrier suffers from less depolarization field and can possess a larger polarization compared with the 2.8 nm PZT barrier.[42]

The room temperature ER observed in our devices is significantly larger than previously reported values for FTJs exploiting single layer tunnel barrier and correlated oxides such as LSMO as electrodes [Fig. 2(c)],[23-25] where the largest RT value is below 100%, observed in a LSMO/2.5 nm PZT/LSMO FTJ.[25] The more than one order of magnitude larger ER reflects the substantial modulation of the electronic states in interfacial $Sr_3Ir_2O_7$ upon polarization switching. It has been shown theoretically that the ER in FTJs results from the asymmetric potential profile seen by tunneling electrons for the opposite polarizations of the tunnel barrier, which is determined by the screening capacity of the electrodes.[30] A high ER is expected when the two electrodes have significantly different screening lengths (δ). For example, about two orders of magnitude enhancement of low temperature tunneling ER has been achieved in FTJs with $BaTiO_3$ tunnel barriers and $La_{0.7}Sr_{0.3}MnO_3$ electrodes by inserting an ultrathin insulating layer of $La_{0.5}Ca_{0.5}MnO_3$ at the interface, where ferroelectric polarization induces an insulating state.[24] In our FTJs, an interfacial insulating state occurs naturally upon polarization switching of PZT. For the 8 nm $LaNiO_3$ layer, the ferroelectric field effect only leads to moderate modulation of metallicity,[35] so we expect thus a similar screening length δ_{LNO} in the P_{up} and P_{down} states. For the Mott insulator $Sr_3Ir_2O_7$, on the other hand, the PZT polarization is sufficient to induce a MIT at the interface [Fig.

2(d)]. In the on (P_{up}) state, hole accumulation in $Sr_3Ir_2O_7$ shifts the Fermi level E_F into the valence band (E_v), resulting in a metallic interface. The corresponding δ_{SIO} is close to δ_{LNO}, leading to high tunneling conductance. In the off (P_{down}) state, hole depletion in interfacial $Sr_3Ir_2O_7$ shifts E_F further into the gap region, leading to a much larger δ_{SIO} compared to δ_{LNO}, which significantly suppresses tunneling conductance. The strong asymmetry in δ modulates the effective tunneling potential profile and hence leads to large ER.

When the temperature is decreased to 100 K, the ER in junction J2 reaches 1.62×10^5%, with the on-state conductance reduced by about 10 and off-state conductance suppression by more than two orders of magnitude. The reduction in I_{on} is likely resulting from the substantially higher contact resistance in the bottom $Sr_3Ir_2O_7$. To quantify this effect, we measured a control device with similar geometry without the junction. The two-point resistance of the device increases from 10^4 Ω at RT to 10^5 Ω at 100 K (Supplementary Fig. S3). The latter becomes comparable with the on-state resistance of the junction, reducing the effectively bias voltage across the junction. This effect is negligible for the off state since the junction resistance is on the order of 10^6 Ω at RT and 10^8 Ω at 100 K, well exceeding the contact resistance. The temperature dependence of I_{off} is thus intrinsic to the junction, suggesting that the off-state transport is not dominated by direct tunneling.

To understand the transport mechanisms, we studied the temperature dependence of tunneling current in junction J3 (4 nm PZT barrier) for both polarization states. We switched the polarization at RT and characterized I vs. V_{bias} at different temperatures. To eliminate the electrode effect, we used the control sample to quantify the contact resistance R_{elec} and deduced the voltage drop across the junction as: $V_j = V_{bias} - I R_{elec}$. Figure 3(a) shows the temperature dependence of tunneling current density $J = I/A$, with A the tunnel barrier area, at $V_j = 0.05$ V. In the P_{up} (on) state, J shows weak temperature dependence, decreasing monotonically from 2.79 nA/μm^2 at 290 K to 2.20 nA/μm^2 at 50 K. According to the Simmons tunneling model for junctions with asymmetric barriers, the J-T relation within the direct tunneling regime can be described by:[46]

$$J(V,T) = J\,(V,0) \times \left\{1 + \frac{6\times10^{-9}\,(sT)^2}{\varphi_1+\varphi_2-V}\right\}. \quad (1)$$

Here, s is the tunneling barrier thickness in the unit of Å, φ_1 and φ_2 denote the smaller and larger barrier height of the asymmetric barrier, respectively, in the unit of volts. Considering that φ_1 and φ_2 are on the order of 1 V, the small decrease of J in the on state can be well described by the direct tunneling model.

In contrast, in the P_{down} (off) state, J decreases monotonically by about two orders of magnitude from 290 K to 50 K, well exceeding that depicted by the direct tunneling model. Figure 3b shows the off-state conductance $G = \frac{dI}{dV}\Big|_{V\to 0}$ as a function of $1/T$. Above 230 K, G increases exponentially with temperature. By fitting to the thermally activated conduction model:

$$G \propto exp\,(-\frac{E_a}{k_B T})\,, \tag{2}$$

where k_B is the Bolzman constant, we deduced an activation energy E_a of 0.29 eV. This activation energy is consistent with previously reported value for PZT,[47] where Pb^{2+} can serve as shallow hole traps for Pb^{3+} with energy level positioned around 0.2 to 0.3 eV above the valence band edge.[48, 49]

Below 230 K, another conduction mechanism with weaker temperature dependence surpasses the thermally activated current. A phenomenon widely observed in FTJs is the defect-mediated inelastic hopping through localized states.[19, 24, 25] The temperature dependence of corresponding tunneling conductance can be described by the Glazman-Matveev (GM) model.[50] Here, the total conductance is the sum of the contributions from all conducting chains through available localized states:

$$G\,(V,T) = G_{DT} + \sum_{N=1}^{\infty} G_N^{hop}(T),\ eV \ll k_B T\,, \tag{3}$$

where G_{DT} is the direct tunneling term and $G_N^{hop}(T)$ characterizes the hopping conductance for going through a given number (N) of localized states. The hopping conductance follows a power-law temperature dependence, $G_N^{hop}(T) = a_N T^{\gamma}$, where a_N is a parameter related to the barrier thickness as well as the density and radius of the localized states, and γ is given by $\gamma(N) = N - \frac{2}{N-1}$. As shown in Fig. 3(b), the GM model can well describe the conductance data from 210 K to 50 K considering $N = 2, 3, 4$. Similar numbers of localized states have been reported for FTJs with ferroelectric oxide barriers of similar thickness.[19]

The different tunneling mechanisms in the on and off states of the FTJ can also be associated with the MIT in interfacial $Sr_3Ir_2O_7$. In the metallic state of $Sr_3Ir_2O_7$, the tunneling behavior is limited by the PZT tunnel barrier, which possesses large bandgap and low defect states, and direct tunneling dominates. As $Sr_3Ir_2O_7$ becomes insulating, the direct tunneling probability decreases

due to the diminishing interfacial density of states. On the other hand, thermally activated carriers in PZT can participate in conduction, with defect-mediated hopping becoming dominant at low temperatures. This scenario is consistent with the weaker temperature dependence of I_{off} observed in device J1 [Fig. 2(a)]. With the thinner PZT barrier, the direct tunneling mechanism remains sizable even in the off state, so the temperature dependence reflects the competing effect of both mechanisms.

Figure 4 shows the cycling behaviors of the FTJs at 50 K. For writing, we applied negative (Write-) and positive (Write+) V_{bias} pulses exceeding V_c of the tunnel barrier to pole PZT into the P_{up} and P_{down} states, respectively [Fig. 4(a)]. Following writing, a small V_{bias} below the V_c was used to read out the tunneling current. Figure 4(b) shows the absolute value of tunnel current $|I|$ for J1 with 2.8 nm PZT upon writing. We have achieved nonvolatile, reversible switching of the tunneling current between the on and off states, with an average ER of 2.3×10^5%. For device J2 with 4 nm PZT, a robust ER of 1.2×10^5% has been achieved [Fig. 4(c)].

In summary, we report nonvolatile, reversible switching of tunneling current in all-oxide FTJs with correlated oxides $LaNiO_3$ and $Sr_3Ir_2O_7$ electrodes. The devices exhibit large ER values of 6,500% at room temperature and over 10^5% at 100 K, which can be attributed to the enhanced potential asymmetry imposed by ferroelectric polarization induced metal-insulator transition in $Sr_3Ir_2O_7$. Our study paves the path for implementing all-oxide FTJs in low power, high density nanoelectronics.

Supplementary Material:

See the supplementary material for the details of sample growth, device fabrication, and additional electrical measurements.

Acknowledgement:

The authors would like to thank Jia Wang for valuable discussions and Qiuchen Wu, Tianlin Li, and Kai Huang for technical support. This work was supported by NSF through Grant No. DMR-1710461 and EPSCoR RII Track-1: Emergent Quantum Materials and Technologies (EQUATE), Award No. OIA-2044049, the UNL Grand Challenges catalyst award entitled Quantum Approaches Addressing Global Threats, and the Nebraska Center for Energy Sciences Research. The research was conducted, in part, at the Nebraska Nanoscale Facility: National Nanotechnology Coordinated Infrastructure and the Nebraska Center for Materials and Nanoscience, supported by the National Science Foundation under Award No. ECCS: 2025298, and the Nebraska Research Initiative.

Conflict of Interest:

The authors have no conflicts to disclose.

Data Availability:

The data that support the findings of this study are available from the corresponding author upon reasonable request.

References:

1 E. Y. Tsymbal and H. Kohlstedt, Tunneling Across a Ferroelectric, Science **313**, 181 (2006).

2 A. Barthélémy, M. Bibes, V. Garcia, A. Gruverman, and E. Y. Tsymbal, Ferroelectric and multiferroic tunnel junctions, MRS Bulletin **37**, 138 (2012).

3 Z. Wen and D. Wu, Ferroelectric Tunnel Junctions: Modulations on the Potential Barrier, Advanced Materials **32**, 1904123 (2020).

4 V. Garcia and M. Bibes, Ferroelectric tunnel junctions for information storage and processing, Nature Communications **5**, 4289 (2014).

5 S. Oh, H. Hwang, and I. K. Yoo, Ferroelectric materials for neuromorphic computing, APL Materials **7**, 091109 (2019).

6 B. B. Tian, J. L. Wang, S. Fusil, Y. Liu, X. L. Zhao, S. Sun, H. Shen, T. Lin, J. L. Sun, C. G. Duan, et al., Tunnel electroresistance through organic ferroelectrics, Nature Communications **7**, 11502 (2016).

7 J. Wu, H.-Y. Chen, N. Yang, J. Cao, X. Yan, F. Liu, Q. Sun, X. Ling, J. Guo, and H. Wang, High tunnelling electroresistance in a ferroelectric van der Waals heterojunction via giant barrier height modulation, Nature Electronics **3**, 466 (2020).

8 X.-W. Shen, Y.-W. Fang, B.-B. Tian, and C.-G. Duan, Two-Dimensional Ferroelectric Tunnel Junction: The Case of Monolayer In:SnSe/SnSe/Sb:SnSe Homostructure, ACS Applied Electronic Materials **1**, 1133 (2019).

9 M. Bibes, J. E. Villegas, and A. Barthélémy, Ultrathin oxide films and interfaces for electronics and spintronics, Adv. Phys. **60**, 5 (2011).

10 C. A. F. Vaz, Y. J. Shin, M. Bibes, K. M. Rabe, F. J. Walker, and C. H. Ahn, Epitaxial ferroelectric interfacial devices, Applied Physics Reviews **8**, 041308 (2021).

11 Y. Yin and Q. Li, A review on all-perovskite multiferroic tunnel junctions, Journal of Materiomics **3**, 245 (2017).

12 C.-L. Jia, S.-B. Mi, K. Urban, I. Vrejoiu, M. Alexe, and D. Hesse, Atomic-scale study of electric dipoles near charged and uncharged domain walls in ferroelectric films, Nature Materials **7**, 57 (2008).

13 J. Hoffman, X. Hong, and C. H. Ahn, Device performance of ferroelectric/correlated oxide heterostructures for non-volatile memory applications, Nanotechnology **22**, 254014 (2011).

14 A. Chanthbouala, V. Garcia, R. O. Cherifi, K. Bouzehouane, S. Fusil, X. Moya, S. Xavier, H. Yamada, C. Deranlot, N. D. Mathur, et al., A ferroelectric memristor, Nature Materials **11**, 860 (2012).

15 M. Gajek, M. Bibes, S. Fusil, K. Bouzehouane, J. Fontcuberta, A. Barthélémy, and A. Fert, Tunnel junctions with multiferroic barriers, Nature Materials **6**, 296 (2007).

[16] V. Garcia, M. Bibes, L. Bocher, S. Valencia, F. Kronast, A. Crassous, X. Moya, S. Enouz-Vedrenne, A. Gloter, D. Imhoff, et al., Ferroelectric Control of Spin Polarization, Science **327**, 1106 (2010).

[17] A. Gruverman, D. Wu, H. Lu, Y. Wang, H. W. Jang, C. M. Folkman, M. Y. Zhuravlev, D. Felker, M. Rzchowski, C. B. Eom, et al., Tunneling Electroresistance Effect in Ferroelectric Tunnel Junctions at the Nanoscale, Nano Letters **9**, 3539 (2009).

[18] V. Garcia, S. Fusil, K. Bouzehouane, S. Enouz-Vedrenne, N. D. Mathur, A. Barthélémy, and M. Bibes, Giant tunnel electroresistance for non-destructive readout of ferroelectric states, Nature **460**, 81 (2009).

[19] Z. Wen, L. You, J. Wang, A. Li, and D. Wu, Temperature-dependent tunneling electroresistance in Pt/$BaTiO_3$/$SrRuO_3$ ferroelectric tunnel junctions, Applied Physics Letters **103**, 132913 (2013).

[20] Z. Wen, C. Li, D. Wu, A. Li, and N. Ming, Ferroelectric-field-effect-enhanced electroresistance in metal/ferroelectric/semiconductor tunnel junctions, Nature Materials **12**, 617 (2013).

[21] H. Lu, A. Lipatov, S. Ryu, D. J. Kim, H. Lee, M. Y. Zhuravlev, C. B. Eom, E. Y. Tsymbal, A. Sinitskii, and A. Gruverman, Ferroelectric tunnel junctions with graphene electrodes, Nature Communications **5**, 5518 (2014).

[22] T. Li, P. Sharma, A. Lipatov, H. Lee, J.-W. Lee, M. Y. Zhuravlev, T. R. Paudel, Y. A. Genenko, C.-B. Eom, E. Y. Tsymbal, et al., Polarization-Mediated Modulation of Electronic and Transport Properties of Hybrid MoS_2–$BaTiO_3$–$SrRuO_3$ Tunnel Junctions, Nano Letters **17**, 922 (2017).

[23] Y. W. Yin, M. Raju, W. J. Hu, X. J. Weng, X. G. Li, and Q. Li, Coexistence of tunneling magnetoresistance and electroresistance at room temperature in $La_{0.7}Sr_{0.3}MnO_3$/(Ba, Sr)TiO_3/$La_{0.7}Sr_{0.3}MnO_3$ multiferroic tunnel junctions, Journal of Applied Physics **109**, 07D915 (2011).

[24] Y. W. Yin, J. D. Burton, Y. M. Kim, A. Y. Borisevich, S. J. Pennycook, S. M. Yang, T. W. Noh, A. Gruverman, X. G. Li, E. Y. Tsymbal, et al., Enhanced tunnelling electroresistance effect due to a ferroelectrically induced phase transition at a magnetic complex oxide interface, Nature Materials **12**, 397 (2013).

[25] Q. H. Qin, L. Äkäslompolo, N. Tuomisto, L. Yao, S. Majumdar, J. Vijayakumar, A. Casiraghi, S. Inkinen, B. Chen, A. Zugarramurdi, et al., Resistive Switching in All-Oxide Ferroelectric Tunnel Junctions with Ionic Interfaces, Advanced Materials **28**, 6852 (2016).

[26] J. Ruan, X. Qiu, Z. Yuan, D. Ji, P. Wang, A. Li, and D. Wu, Improved memory functions in multiferroic tunnel junctions with a dielectric/ferroelectric composite barrier, Applied Physics Letters **107**, 232902 (2015).

[27] L. Chen, Y. Feng, Y. Chen, Y. Chen, R. Liu, D. Pan, P. Wang, Y. Xu, R. Zhang, and X. Wang, Enhancement of tunneling electroresistance by interfacial cation intermixing in ferroelectric tunnel junctions, Applied Surface Science **512**, 145707 (2020).

[28] Y. Wang, Q. Zhang, J. Zhou, J. Liu, Z. Ma, P. Zhou, T. Zhang, and N. Valanoor, Fowler–Nordheim tunneling-assisted enhancement of tunneling electroresistance effect through a composite barrier, Applied Physics Letters **116** (2020).

[29] L. Chen, J. Zhou, X. Zhang, K. Ding, J. Ding, Z. Sun, and X. Wang, Low-Temperature Tunneling Electroresistance in Ferromagnetic Metal/Ferroelectric/Semiconductor Tunnel Junctions, ACS Applied Materials & Interfaces **13**, 23282 (2021).

[30] M. Y. Zhuravlev, R. F. Sabirianov, S. S. Jaswal, and E. Y. Tsymbal, Giant Electroresistance in Ferroelectric Tunnel Junctions, Physical Review Letters **94**, 246802 (2005).

[31] H. Yamada, M. Marinova, P. Altuntas, A. Crassous, L. Bégon-Lours, S. Fusil, E. Jacquet, V. Garcia, K. Bouzehouane, A. Gloter, et al., Ferroelectric control of a Mott insulator, Scientific Reports **3**, 2834 (2013).

[32] Y. Hao, T. Li, Y. Yun, X. Li, X. Chen, J. Song, Z. Ahmadi, J. E. Shield, X. Xu, and X. Hong, Tuning Negative Capacitance in $PbZr_{0.2}Ti_{0.8}O_3/SrTiO_3$ Heterostructures via Layer Thickness Ratio, Physical Review Applied **16**, 034004 (2021).

[33] X. Hong, A. Posadas, and C. H. Ahn, Examining the screening limit of field effect devices via the metal-insulator transition, Applied Physics Letters **86**, 142501 (2005).

[34] L. Zhang, X. G. Chen, H. J. Gardner, M. A. Koten, J. E. Shield, and X. Hong, Effect of strain on ferroelectric field effect in strongly correlated oxide $Sm_{0.5}Nd_{0.5}NiO_3$, Applied Physics Letters **107**, 152906 (2015).

[35] Y. Hao, X. Chen, L. Zhang, M.-G. Han, W. Wang, Y.-W. Fang, H. Chen, Y. Zhu, and X. Hong, Record high room temperature resistance switching in ferroelectric-gated Mott transistors unlocked by interfacial charge engineering, Nature Communications **14**, 8247 (2023).

[36] S. J. Moon, H. Jin, K. W. Kim, W. S. Choi, Y. S. Lee, J. Yu, G. Cao, A. Sumi, H. Funakubo, C. Bernhard, et al., Dimensionality-Controlled Insulator-Metal Transition and Correlated Metallic State in 5*d* Transition Metal Oxides $Sr_{n+1}Ir_nO_{3n+1}$ (n=1, 2, and ∞), Physical Review Letters **101**, 226402 (2008).

[37] H. J. Park, C. H. Sohn, D. W. Jeong, G. Cao, K. W. Kim, S. J. Moon, H. Jin, D.-Y. Cho, and T. W. Noh, Phonon-assisted optical excitation in the narrow bandgap Mott insulator $Sr_3Ir_2O_7$, Physical Review B **89**, 155115 (2014).

[38] R. G. Palgrave, P. Borisov, M. S. Dyer, S. R. C. McMitchell, G. R. Darling, J. B. Claridge, M. Batuk, H. Tan, H. Tian, J. Verbeeck, et al., Artificial Construction of the Layered Ruddlesden–Popper Manganite $La_2Sr_2Mn_3O_{10}$ by Reflection High Energy Electron Diffraction Monitored Pulsed Laser Deposition, Journal of the American Chemical Society **134**, 7700 (2012).

[39] G. Cao, S. McCall, M. Shepard, J. E. Crow, and R. P. Guertin, Magnetic and transport properties of single-crystal Ca_2RuO_4: Relationship to superconducting Sr_2RuO_4, Physical Review B **56**, R2916 (1997).

[40] R. Liu, L. Si, W. Niu, X. Zhang, Z. Chen, C. Zhu, W. Zhuang, Y. Chen, L. Zhou, C. Zhang, et al., Light-Induced Mott-Insulator-to-Metal Phase Transition in Ultrathin Intermediate-Spin Ferromagnetic Perovskite Ruthenates, Advanced Materials **35**, 2211612 (2023).

[41] T. Li, H. Chen, K. Wang, Y. Hao, L. Zhang, K. Watanabe, T. Taniguchi, and X. Hong, Transport Anisotropy in One-Dimensional Graphene Superlattice in the High Kronig-Penney Potential Limit, Physical Review Letters **132**, 056204 (2024).

[42] C. Lichtensteiger, J.-M. Triscone, J. Junquera, and P. Ghosez, Ferroelectricity and Tetragonality in Ultrathin $PbTiO_3$ Films, Physical Review Letters **94**, 047603 (2005).

[43] K. Wang, Y. Hao, L. Zhang, Y. Zhang, X. Chen, and X. Hong, Effect of correlated oxide electrodes on disorder pinning and thermal roughening of ferroelectric domain walls in epitaxial $PbZr_{0.2}Ti_{0.8}O_3$ thin films, Physical Review Materials **5**, 074402 (2021).

[44] Q. Wu, K. Wang, A. Simpson, Y. Hao, J. Wang, D. Li, and X. Hong, Electrode Effect on Ferroelectricity in Free-Standing Membranes of $PbZr_{0.2}Ti_{0.8}O_3$, ACS Nanoscience Au **3**, 482 (2023).

[45] G. Radaelli, D. Gutiérrez, F. Sánchez, R. Bertacco, M. Stengel, and J. Fontcuberta, Large Room-Temperature Electroresistance in Dual-Modulated Ferroelectric Tunnel Barriers, Advanced Materials **27**, 2602 (2015).

[46] J. G. Simmons, Generalized Thermal J-V Characteristic for the Electric Tunnel Effect, Journal of Applied Physics **35**, 2655 (1964).

[47] P. C. Juan, H. C. Chou, and J. Y. M. Lee, The effect of electrode material on the electrical conduction of metal-$Pb(Zr_{0.53}Ti_{0.47})O_3$-metal thin film capacitors, Microelectronics Reliability **45**, 1003 (2005).

[48] J. Robertson, W. L. Warren, B. A. Tuttle, D. Dimos, and D. M. Smyth, Shallow Pb^{3+} hole traps in lead zirconate titanate ferroelectrics, Applied Physics Letters **63**, 1519 (1993).

[49] P. F. Baude, C. Ye, and D. L. Polla, Deep level transient spectroscopy characterization of ferroelectric $Pb(Zr,Ti)O_3$ thin films, Applied Physics Letters **64**, 2670 (1994).

[50] L. I. Glazman and K. A. Matveev, Inelastic tunneling across thin amorphous films, Soviet Journal of Experimental and Theoretical Physics **67**, 1276 (1988).

Figures:

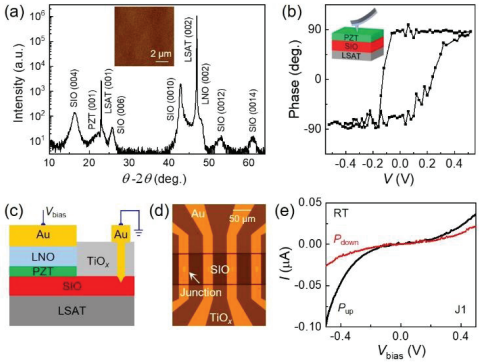

FIG. 1. (a) XRD θ-2θ scan taken on 8 nm LNO/4 nm PZT/20 nm SIO on LSAT. Inset: AFM image of the sample. (b) PFM phase switching hysteresis taken on 4 nm PZT/12 nm SIO. Inset: Sample schematic. (c) Schematic FTJ cross-section. (d) Optical image of a sample patterned with four tunnel junctions. (e) I-V_{bias} of junction J1 at RT.

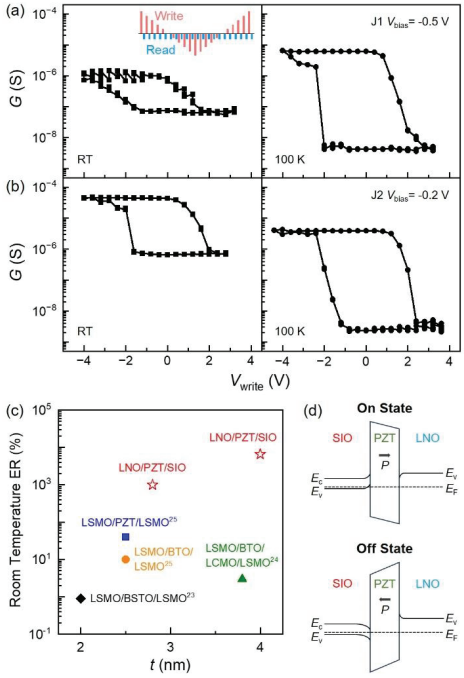

FIG. 2. *G vs.* V_{write} at RT and 100 K for (a) J1 (2.8 nm PZT), and (b) J2 (4 nm PZT). Inset: Schematic of the writing/reading V_{bias} sequence. (c) ER *vs. t* at RT taken on various all-oxide FTJs. Open symbols: present study. Solid symobols: data from Refs. [23-25]. BTO: $BaTiO_3$. BSTO: $(Ba,Sr)TiO_3$. LCMO: $(La,Ca)MnO_3$. (d) Schematic band diagrams of the FTJ in the on and off states.

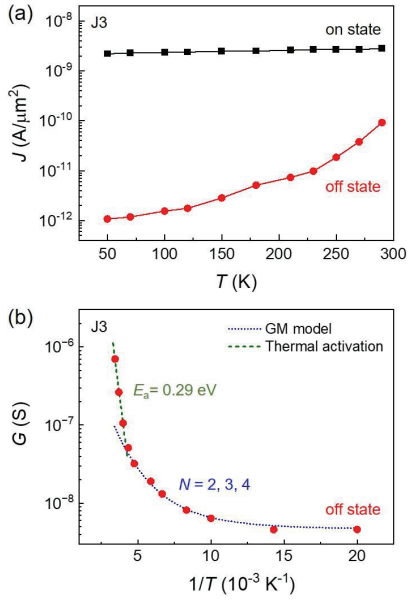

FIG. 3. (a) J *vs*. T at $V_{bias} = 0.05$ V for both polarization states, and (b) G *vs*. $1/T$ of the off state for J3 with 4 nm PZT barrier.

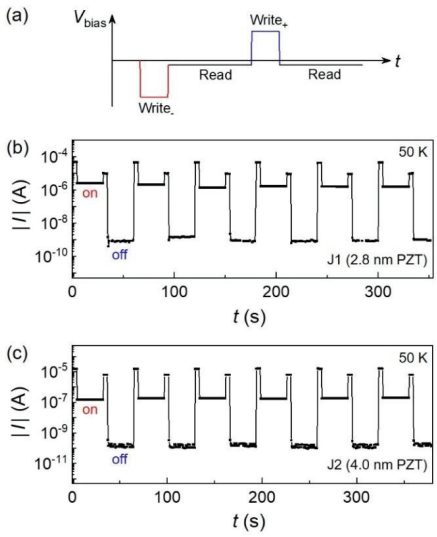

FIG. 4. (a) Schematic of the V_{bias} sequence. (b-c) $|I|$ *vs*. t upon the application of V_{bias} pulses for junctions J1 (b) and J2 (c) at 50 K. The write$_-$ (write$_+$) voltages are -4 V (+3.2 V) for J1 and -4 V (+3 V) for J2.